Communications in Science and Technology 10(1) (2025) 170–178

COMMUNICATIONS IN
SCIENCE AND TECHNOLOGY
Homepage: cst.kipmi.or.id

Optimizing ground control points for UAV photogrammetry: a case study in slope stability mapping

Muhammad Hafizhir Ridha[a], Yulian Firmana Arifin[a,*], Ari Surya Abdi[b]

[a]*Department of Civil Engineering, University of Lambung Mangkurat, Banjarmasin 70123, Indonesia*
[b]*Department of Civil Engineering, National Taiwan University, Taipei 106319, Taiwan*

Article history:
Received: 26 December 2024 / Received in revised form: 13 June 2025 / Accepted: 15 June 2025

Abstract

This study investigated the effect of Ground Control Point (GCP) distribution on the accuracy of UAV-based slope mapping and stability analysis. Three GCP configurations—top-only, vertical, and diagonal—were tested. Accuracy was evaluated using UAV photogrammetry and compared to GPS geodetic data. The vertical GCP setup produced the highest accuracy, reducing total RMSE by 89.6% (from 52.93 mm to 5.50 mm). The diagonal configuration, while being slightly less accurate (61.26 mm RMSE), improved spatial coverage. Slope stability analysis using the finite element method (FEM) confirmed the reliability of the vertical setup for slope assessment. These results demonstrated that optimizing GCP layout could significantly improve model precision while reducing fieldwork. This work contributes to efficient and accurate slope monitoring with fewer GCPs, making it suitable for large-scale geotechnical applications. Future research will focus on applying these configurations to vegetated and more complex terrains and integrating automation for broader and scalable implementation.

Keywords: UAV photogrammetry; Ground Control Points (GCP); slope stability; disaster risk management

---

1. Introduction

Unmanned aerial vehicle (UAV) photogrammetry has transformed geospatial mapping and slope stability studies by providing efficient high-resolution terrain analyses, particularly for complex and hazardous area. UAVs equipped with real-time kinematic (RTK) and post-processing kinematic (PPK) GNSS systems deliver precise spatial data that are critical for geotechnical assessments [1]. The use of RGB, thermal, and LiDAR sensors also enhances 3D mapping in disaster-prone environments [2].

Accurate digital elevation models (DEMs) and surface models (DSMs) are crucial for identifying vulnerable slopes and enabling early landslides warning [3]. UAV data, when combined with geophysical imaging and finite element method (FEM) analysis, can improve embankment stability evaluation and supported risk mitigation strategies [4,5].
However, achieving high accuracy in complex terrains requires cautious consideration of ground control points (GCP) placement, which greatly influences the root mean square error (RMSE) of elevation models [6,7].

Strategic GCP placement remains a logistical challenge, particularly in accessible slope zones. Reducing the GCP usage without compromising its accuracy remains the key research goal. In this regard, GPS geodetic methods offer a reliable benchmarks and support UAV validation [8–11].

Accurate soil data from field tests, including cone penetration tests (CPT) and boring tests, further support slope stability modeling. CPT provide continuous soil resistance profiles that correlate with geotechnical parameters such as density, shear strength, and internal friction angle without disturbing the soil structure [17-19]. Laboratory analyses refine the field data and ensure precise cohesion and moisture content measurements, which are essential for predicting the slope behavior under various conditions [20-22]

This study explored the feasibility of minimizing GCPs in UAV-based slope photogrammetry while maintaining model accuracy through validation with GPS geodetic data and FEM analysis, supported by soil data from CPT and boring tests. Vertical and diagonal GCP configurations were tested against geodetic benchmarks to enhance slope modeling with reduced field intervention.

Although existing studies have explored GCP reduction, few have integrated GCP optimization with geotechnical validation using subsurface data and FEM modeling. Unlike previous studies, which mostly assessed spatial accuracy, this research introduces a novel validation framework that links sparse GCP configurations with slope safety modeling using FEM. This integrative approach fills a gap in the literature concerning GCP

---

* Corresponding author. Tel.: +62-511-4773858; fax: +62-511-4773858.
Email: y.arifin@ulm.ac.id
https://doi.org/10.21924/cst.10.1.2025.1627

minimization strategies for complex slope environments and offers practical insights for geotechnical risk assessment and disaster mitigation.

2. Materials and Methods

2.1. Site background

A topographic survey was performed at Tebing Pandang in Benua Riam Village, Aranio District, Banjar Regency, South Kalimantan. This area, covering approximately 0.9 hectares, features a hilly terrain with steep slopes and sharp elevation changes, which renders it particularly vulnerable to slope instability. Loose, easily eroded soil, and weathered rock increase the risk of landslides, especially during heavy rainfall, increasing the pore water pressures. Although the local vegetation provides some stabilization, human activities and poor drainage exacerbate these risks. The challenging topography, soil composition, and high rainfall conditions highlight the need for an effective slope management. The survey coordinates were recorded at 50M 283279.9614818, oriented at 346° North that provided essential data for further slope stability assessment and management.

2.2. Tools and equipment used

Specialized equipment was employed to achieve high-precision geospatial mapping and slope stability analysis. The Comnav T300 RTK Geodetic GPS provided accurate positioning for GCPs, which is essential for enhancing the UAV photogrammetry accuracy in difficult conditions [8]. Meanwhile, the DJI Phantom 4 Professional Obsidian UAV equipped with GNSS and high-resolution imaging enabled efficient data capture and created detailed 3D models for stability assessments [1]. For soil profiling, a 2.5-ton CPT device provided continuous resistance data to determine the soil shear strength, whereas hand boring facilitated the laboratory analysis of cohesion, moisture content, and other critical parameters in slope stability modeling [4]. This integrated approach, as illustrated in Fig. 1, outlines the workflow from the benchmark (BM) and GCP setups to the UAV data collection and two-dimensional (2D) modeling for a comprehensive slope stability analysis.

2.3. UAV and GPS geodetic data acquisition

The initial step in data collection involved establishing benchmark (BM) points using RTK Geodetic GPS to provide elevation references and accurate coordinates (East and South) throughout the study area. The Comnav T300 RTK Geodetic GPS ensured the precise positioning of the BM points, which anchored all subsequent UAV measurements to a consistent geospatial framework, which is vital for slope stability analysis [8]. Each GCP used in the photogrammetry was also established by means of RTK GPS to ensure accurate alignment with the BM reference framework. Fig. 2 illustrates the setup of the BM and GCPs, which demonstrates the use of a geodetic GPS to achieve high-accuracy mapping.

2.4. UAV data collection and GCP configurations

The DJI Phantom 4 Professional Obsidian UAV was flown at a fixed altitude of 50 m above the ground and captured high-resolution images necessary for constructing DSMs and DEMs. The UAV flight paths were predefined to comprehensively cover the study area, thereby ensuring detailed imagery over both steep and flat terrain. In this study, the GCPs, as shown in Fig. 3, were strategically placed in three unique configurations at three points each to assess their impact on model accuracy: (1) at the top of the slope, (2) in a straight line down the slope, and (3) arranged diagonally on the slope. While previous research demonstrated the importance of the GCP distribution for model precision [6], these specific configurations were developed to enhance the accuracy of the challenging topography of the study area.

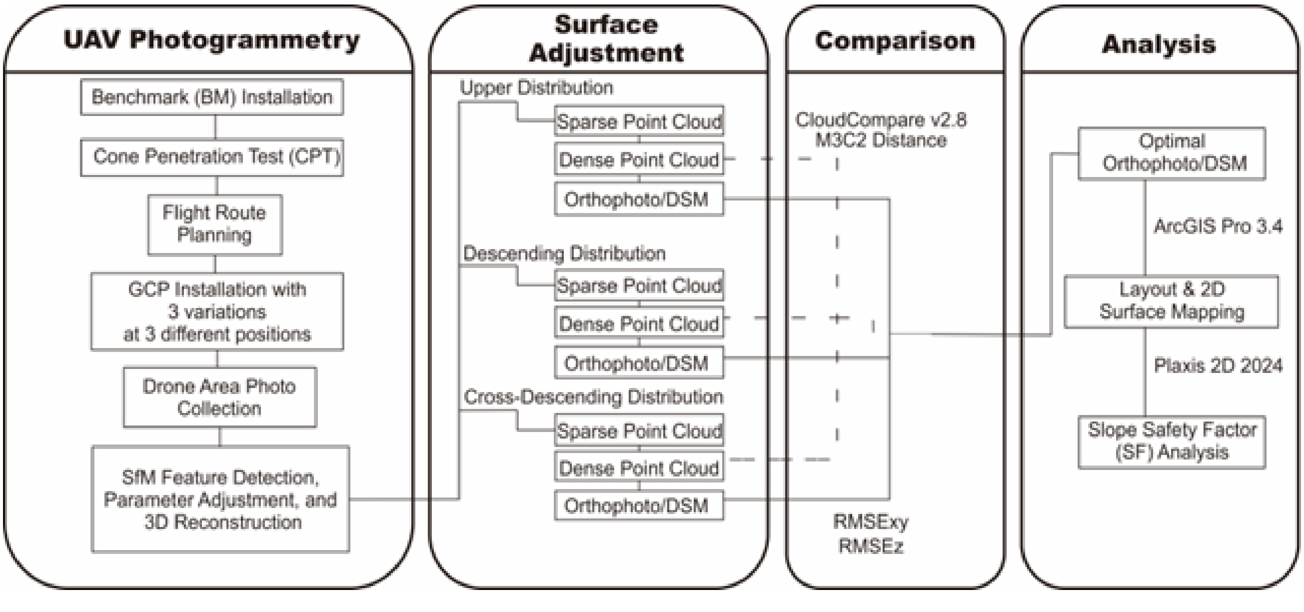

Fig. 1. Workflow diagram for UAV-based photogrammetry and slope stability analysis using GCP configurations and FEM modeling

Fig. 2. Establishing benchmarks (BM) and ground control points (GCP) using geodetic GPS for high-precision mapping.

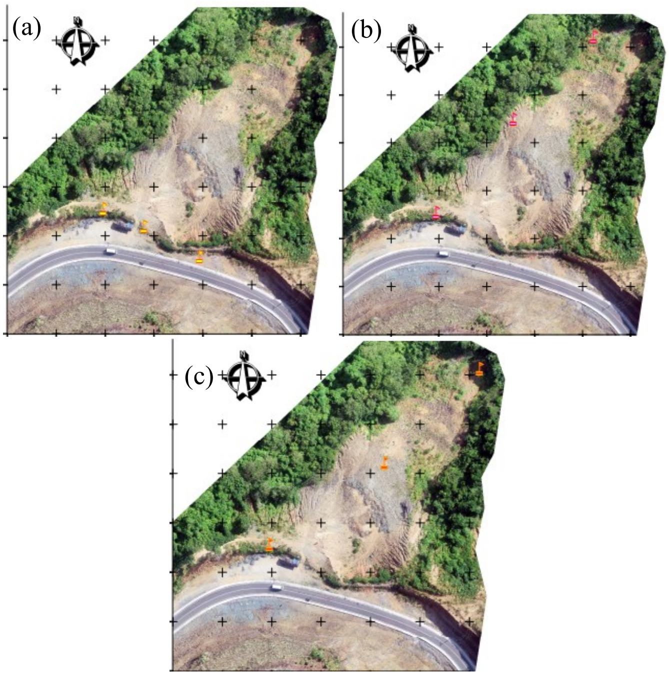

Fig. 3. GCP placement configurations: (a) Top, (b) Straight, and (c) Diagonal on slope

2.5. Photogrammetric processing

The photogrammetric process started with UAV data to create DSMs and DEMs using Agisoft MetaShape. The initial steps included feature detection, alignment, and dense point cloud generation, followed by 3D model reconstruction and texture mapping to enhance the model detail and accuracy [1]. The DSM and DEM models were further refined using CloudCompare to align and calibrate the point clouds precisely [3]. ArcGIS was used to produce topographic maps, which provided a comprehensive view of the slope area essential for accurate slope analysis [5].

2.6. Accuracy assessment

The reliability of the photogrammetric models was evaluated through an accuracy assessment using root mean square error (RMSE) metrics for both the horizontal (RMSExy) and vertical (RMSEz) dimensions. This assessment quantified the spatial accuracy of the DSM and DEM across different GCP configurations. Furthermore, UAV-derived slope contours were compared with geodetic GPS reference measurements to evaluate the precision [14]. This comparison helped to determine the effect of the GCP distribution on model accuracy and establish a benchmark for UAV-based mapping effectiveness in geotechnical applications [6].

This integrated workflow, which combined RTK GPS, UAV photogrammetry, and advanced data processing, ensured that the slope stability models were accurate and reliable. By aligning the UAV data with geodetic GPS measurements, this study highlighted the potential of UAV photogrammetry for precise mapping and stability assessment of complex terrains, thus supporting disaster risk management and geotechnical analysis in vulnerable areas [9].

2.7. Soil testing and laboratory analysis

Field soil testing included CPT and hand boring tests, which are essential for collecting soil parameters for finite element modeling in slope stability analysis. Following the Indonesian National Standard (SNI) 8460-2017, soil testing was performed at three locations: the top, middle, and base of the slope. The CPT and hand boring tests were performed 2 m apart as specified by the standard. Undisturbed soil samples were taken at the depths of 2.4-2.8 m at Point S-1 (top), 1.5-2.0 meters at Point S-2 (middle), and 1.6-2.0 meters at Point S-3 (base). These samples were tested for cohesion, moisture content, Atterberg limits, and shear strength to ensure an accurate representation of soil conditions in stability modeling.

2.8. Finite element slope stability analysis

In this study, the slope stability was assessed using the two-dimensional (2D) FEM Plaxis software in which the model geometry was constructed based on the generated DEM/DSM models. The models served as the basis for simulating the slope geometry and stratification with soil parameters such as cohesion, internal friction angle, and moisture content obtained from the CPT and hand-boring tests [4]. A medium-density mesh was used with fixed boundaries at the base and vertical roller conditions on the lateral sides. Although no field deformation data were available for calibration, all models shared identical soil inputs, allowing for a valid comparative analysis between GCP-derived geometries. The analysis calculated the safety factors and identified the potential failure zones by leveraging FEM-based modeling methods as validated in previous studies [15]. UAV and GPS geodetic data were used to verify the slope geometry and assess its stability in order to facilitate a detailed slope-failure risk evaluation.

3. Results and Discussions

3.1. Impact of GCP distribution and accuracy metrics in UAV photogrammetry

Table 1 presents a comparison of the accuracy of UAV photogrammetry processed using Agisoft Metashape for three different GCP configurations: top-only, straight vertical, and diagonal distribution. The metrics analyzed included ground sampling distance (GSD), vertical (Z), horizontal (XY), and total errors. These RMSE values were computed by Agisoft Metashape based on deviations between the model and control points, and the large difference between configurations reinforced the superior accuracy of the vertical GCP setup.

Table 1. Accuracy metrics (GSD, RMSEz, RMSExy, RMSEtotal) for three GCP configurations in UAV photogrammetry processed with Agisoft Metashape

Type	GSD (mm/pixel)	RMSEz (mm)	RMSE xy (mm)	RMSE total (mm)
3 GCPs Positioned at the Top	16.2	17.29	50.03	52.93
3 GCPs Positioned in a Straight Vertical Line from Top to Bottom	16	0.69	5.46	5.50
3 GCPs Positioned Diagonally from Top to Bottom	16	14.24	59.58	61.26

The top-only GCP configuration yielded the highest total error (52.93 mm), largely due to insufficient control in lower slope areas, highlighting its unsuitability for precise mapping. This finding supports prior studies noting the poor performance of clustered GCPs at higher elevations [7][16].

In contrast, the vertical configuration produced the lowest total error (5.50 mm), representing an 89.6% reduction compared to the top-only configuration. This aligns with Seo et al. [16], who stressed the effectiveness of vertical GCP distribution in reducing elevation and total error. Nevertheless, its limited horizontal spread could constrain performance in more complex terrains.

The diagonal setup, though exhibiting a higher total error (61.26 mm), offered a broader spatial coverage, effectively capturing both vertical and horizontal features. This trade-off between spatial coverage and precision reflects the findings by Martínez-Carricondo et al. [7] and Seo et al. [16] that emphasized the value of diagonal GCP placement in representing terrain variability.

3.2. Multiscale 3D distance analysis of GCP configurations

The Multiscale Model to Model Cloud Comparison (M3C2) distance analysis was employed to quantify elevation discrepancies between UAV-derived point clouds and GPS geodetic benchmarks for three different GCP configurations. In the top-only GCP setup (Fig. 4), significant overestimations in elevation were observed, particularly in the lower slope regions. This is indicated by the dominant red and yellow tones, reflecting deviations exceeding +3 meters. These errors highlight the limitations of clustered GCP placement in capturing full slope variability, in line with prior studies by Seo et al. [16] and Gindraux et al. [17].

The vertical GCP configuration (Fig. 5) demonstrated improved elevation accuracy, as evidenced by widespread green and blue zones. These colors indicate smaller elevation differences, generally within ±2.5 meters, especially in the lower portions of the slope. Although minor horizontal discrepancies remained, the vertical arrangement significantly reduced vertical errors, supporting the conclusions of Seo et al. [16] on the benefits of vertically aligned GCPs.

In the diagonal GCP configuration (Fig. 6), the slope surface exhibited a more consistent pattern of green and grey tones. These corresponded to a narrow band of elevation differences centered around zero, suggesting a closer match between UAV and GPS models across both horizontal and vertical axes. The broader spatial coverage and balanced alignment offered by the diagonal setup reinforce the findings of Martínez-Carricondo et al. [7], who advocated for diagonal GCP layouts in complex terrain to enhance DEM reliability.

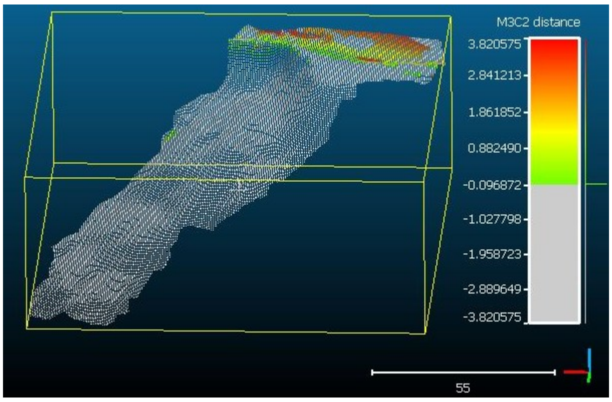

Fig. 4. M3C2 distance analysis for top-only GCP configuration

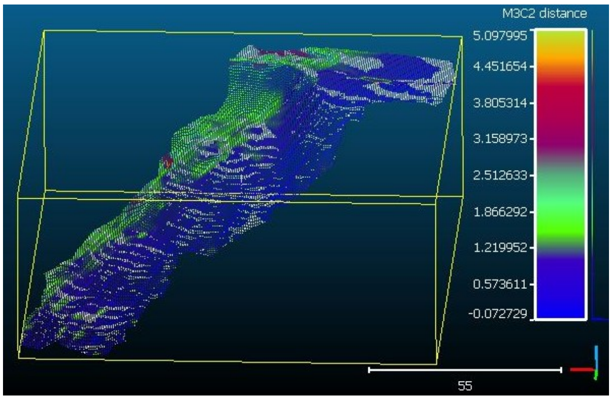

Fig. 5. M3C2 distance analysis for vertical GCP configuration

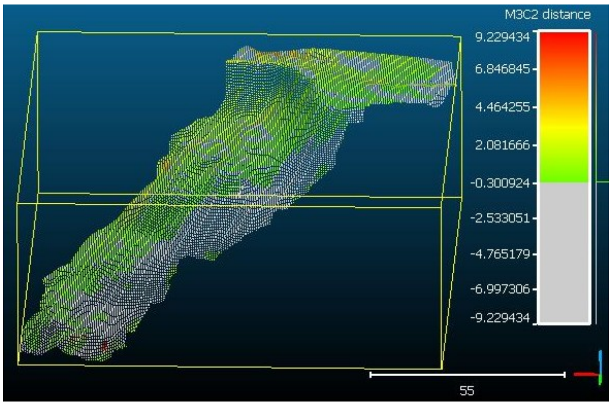

Fig. 6. M3C2 Distance analysis for diagonal GCP configuration

3.3. Cross-sectional analysis of slope profiles based on GCP configurations

Fig. 7(a) illustrates a top view of the studied slope with cross-sectional lines to visualize the accuracy of the GCP placements. Meanwhile, Fig. 7(b–d) present the slope profiles generated using ArcGIS, comparing different GCP configurations (GPS geodetic data, top-only GCPs, straight-line GCPs, and diagonal GCPs) against the GPS baseline.

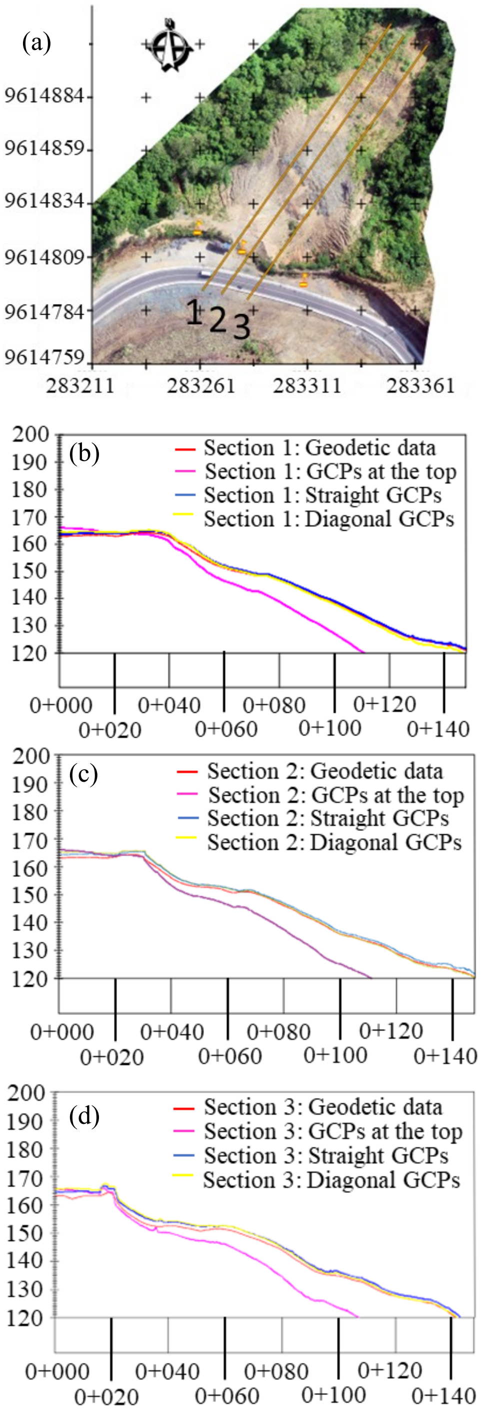

Fig. 7. Cross-sectional analysis of slope: (a) cross-section positions, (b) cross-section 1, (b) cross-section 2, and (d) cross-section 3

In Fig. 7(b) (Section 1), the top-only GCPs showed significant deviations, whereas the straight-line GCPs improved the accuracy, and the diagonal GCPs aligned best with the GPS baseline. Fig. 7(c) (Section 2) and Fig. 7(d) (Section 3) show the similar patterns where the diagonal GCPs consistently offered superior accuracy compared to the top-only configuration.

These results emphasized the importance of well-distributed GCPs for accurate slope modeling, particularly in complex terrain. The diagonal GCP arrangement provided the best spatial coverage and aligned closely with the GPS data. These findings align with those of previous studies by Carvajal-Ramírez et al. [18], Martínez-Carricondo et al. [7], and Seo et al. [16], thereby highlighting the role of strategic GCP placement in improving the accuracy of UAV photogrammetry. In this case, ArcGIS played a crucial role in visualizing these differences in geospatial applications.

3.4. Soil data and subsurface layering

CPT data from three slope points (Fig. 8) revealed moderate variations in cone resistance (q_c) and friction ratio (FR) along depth. CPT 1 displayed lower q_c values near the surface (0–0.6 m), while CPT 3 showed slightly elevated resistance at 2.2–4 m depth, suggesting heterogeneity in near-surface materials. All locations identified a hard soil layer between 9.8 and 10.6 m, indicating the relatively uniform base stratigraphy. Overall, FR profiles aligned across sites, except at CPT 1 (0–1.8 m) and CPT 3 (1.8–4.0 m) where deviations indicated localized transitions in soil behavior.

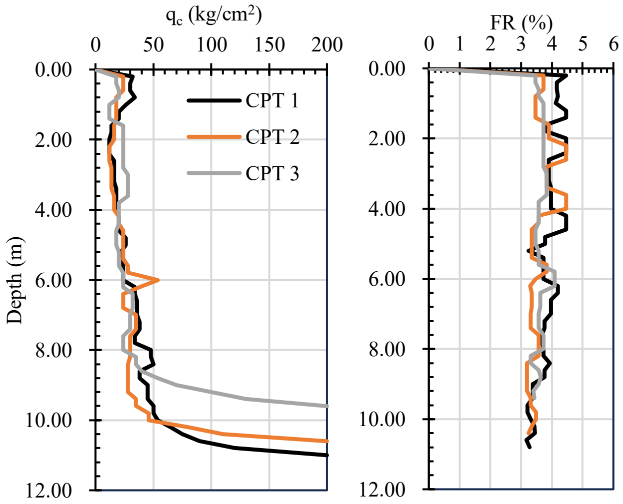

Fig. 8. Cone penetration test (CPT) results: cone resistance (q_c) and friction ratio (FR) profiles for CPT 1, CPT 2, and CPT 3

Soil classification based on the Robertson chart (Fig. 9a) showed zones 3–6, ranging from cohesive clay to silty sand. This gradation indicated increasing drainage and decreasing plasticity from deeper to shallower layers. Subsurface stratigraphy (Fig. 9b) confirmed layered compositions: clay (Layer 3), silty clay (Layer 4), clay silt (Layer 5), and sandy silt (Layer 6). These layers informed FEM modeling by representing the vertical heterogeneity critical to slope response under loading.

Laboratory tests (Table 2) further supported this stratification. BH3 exhibited the highest unit weight and stiffness with a modulus of elasticity (E_u) of 2178 kN/m², suggesting denser and more competent soils. In contrast, BH1 showed the highest moisture content (20.89%) and lowest strength, consistent with more plastic, compressible materials. Variations in cohesion (44.18–51.44 kN/m²) and internal friction angle (18.47°–19.38°) provided essential inputs for FEM stability assessments. This combination of CPT profiling and borehole analysis enabled a robust geotechnical understanding of the slope, vital for accurate numerical modeling.

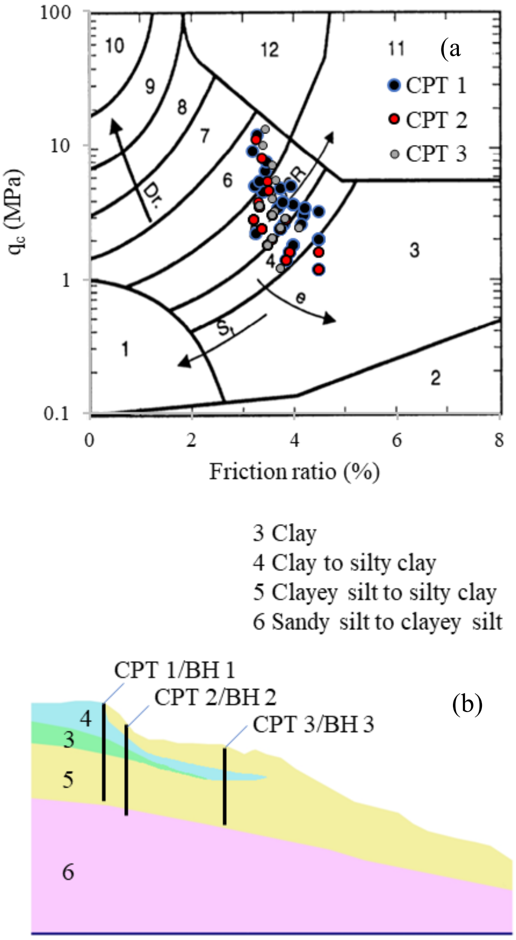

Fig. 9. (a) Soil classification at locations 1, 2, and 3 using CPT data and (b) soil stratigraphy prediction based on CPT data

The laboratory results further showed subsurface variability. Silt dominated the grain size distribution, while clay content varied modestly among boreholes. BH2 showed the highest plasticity index (19.63%), suggesting greater deformability, whereas BH3 exhibited the highest shear strength and stiffness, with the cohesion of 51.44 kN/m², unconfined compressive strength of 108.88 kN/m², and modulus of elasticity reaching 2178 kN/m². These contrasts confirm the heterogeneity of the slope's mechanical properties, a critical factor for accurate modeling in slope stability analysis.

3.5. FEM modeling for slope stability

Previous studies [27-29] revealed that the use of CPT data for estimating soil properties requires region-specific empirical correlations, particularly when the laboratory-based results are not readily available. Niazi [19] highlighted that the methods outlined in his manual were designed specifically for Indiana's geology where extensive CPT research has been performed to ensure the reliability of the results. Zhou et al. [20] developed regional correlations in New Zealand and demonstrated a need to adapt CPT-based estimations for local soil types by comparing CPT data with Standard Penetration Test (SPT), Dilatometer Test (DMT), and shear wave velocity (Vs) measurements. Similarly, Tamošiūnas et al. [21] presented correlations for Young's modulus and other moduli in Lithuania, emphasizing the need for region-specific equations to ensure accurate results in varying soil conditions. Therefore, for greater accuracy, the current study sought to establish localized empirical correlations between the CPT data and the laboratory-based soil properties for the study area, as summarized in Table 3.

Table 2. Soil properties from BH1, BH2, and BH3 for slope stability analysis

Properties		BH 1	BH 2	BH 3
Depth	(m)	1.60-2.00	2.20-2.60	2.20-2.60
water content	(%)	20.89	18.13	17.36
Specific gravity		2.668	2.672	2.68
Unit weight (γ)	kN/m^3	16.81	16.87	17.01
Gravel	(%)	3.13	2.41	3.66
Coarse sand	(%)	6.28	5.74	6.85
Medium sand	(%)	4.72	4.05	4.8
Fine sand	(%)	5.39	5.5	5.39
Silt	(%)	67.29	68.29	69.39
Clay	(%)	13.19	14.01	9.91
Liquid limit (LL)	(%)	45.5	46.63	44.6
Plastic limit (PL)	(%)	26.41	27.01	16.18
Plasticity index (PI)	(%)	19.47	19.63	18.41
Soil classification (USCS)		ML	ML	ML
Cohesion (c)	kN/m^2	44.18	47.5	51.44
Internal friction angle (ϕ)	(°)	18.47	19.38	19.02
Unconfined compressive strength (q_u)	kN/m^2	80.7	92.7	108.88
Modulus elasticity (E_u)	kN/m^2	1464	1710	2178

Table 3. Empirical Relationship Between Soil Parameters and CPT Results Used in FEM analysis

Parameter	Correlation	r^2
Unit weight (kN/m^3)	$\gamma = 0.0168q_c + 16.606$	0.99
Cohesion (kN/m^2)	$c = 10.364\ln(q_c) + 18.552$	0.99
Internal friction angle (°)	$\phi = 24.342\ FR^{-0.185}$	0.98
Modulus elasticity (kN/m^2)	$E = 59.315q_c + 755.84$	0.99

3.6. Slip surface and slope safety factor analysis

Fig. 10 presents the results of the slope stability analysis performed using Plaxis by comparing the slopes with three different GCPs positioned in various configurations, as previously described. Fig. 10(a), (b), (c), and (d) show the slopes with three GCPs placed at the top, placed diagonally along the slope, arranged in a straight line along the slope, and the GPS geodetic reference, used as the baseline for comparison. The color gradient in the figures represents the distribution of shear strain; warmer colors (red to yellow) indicate the areas of higher strain and potential instability, whereas the cooler colors (blue) represent stable regions.

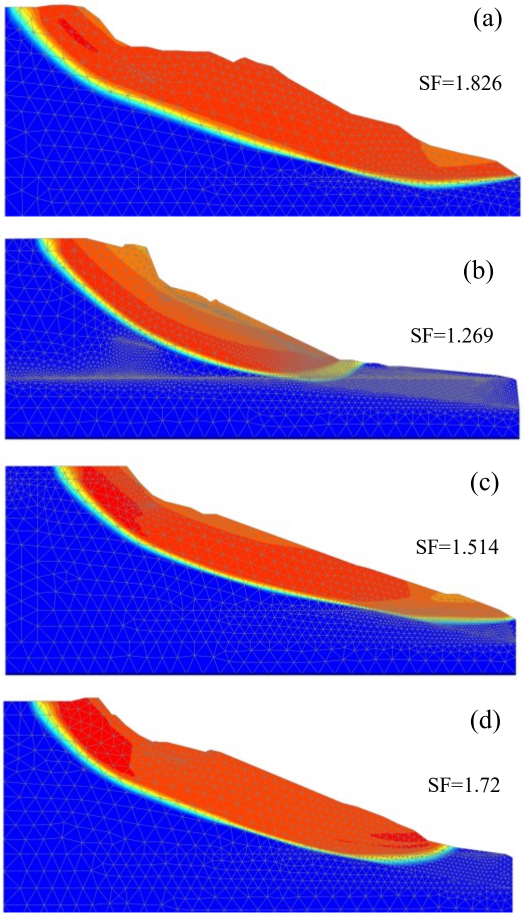

Fig. 10. Slope stability analysis with different GCP configurations: (a) GPS geodetic baseline, (b) three GCPs at the top, and (c) three diagonal GCPs. (d) 3 GCPs in a straight line

The safety factor (SF) for each slope configuration was calculated as follows: 1.269 for the top-only GCPs, 1.514 for the diagonal GCPs, 1.72 for the straight-line GCPs, and 1.826 for the GPS geodetic reference. A comparison of the three analyzed slope models with the GPS Geodetic reference (SF = 1.826) revealed differences in slope stability and strain distribution based on GCP placement. The first slope with three GCPs concentrated at the top achieved an SF of 1.269, indicating a moderate stability with limited safety margins. The strain was concentrated near the crest and upper sections of the slope, suggesting a higher risk of localized instability. This configuration was the least stable among the models and significantly underperformed the GPS Geodetic reference.

The second slope with the GCPs placed diagonally from top to bottom had a higher SF of 1.514. This configuration provided a more balanced strain distribution, resulting in improved stability. Although this was better than the top-only GCP model, it still differed from the GPS Geodetic reference, indicating room for further optimization. The third slope with the GCPs aligned vertically along the center of the slope achieved the highest SF of 1.72; it indicated that the strain distribution became more evenly spread. As the SF approached the GPS Geodetic reference of 1.826, the characteristics of the slope behavior became more similar, indicating that this model yielded results closer to the geodetic data.

3.7. Contribution to disaster risk management

This study contributes to disaster risk management by improving the efficiency and accuracy of landslide mapping and slope-stability analyses. It aims to reduce the number of Ground Control Points (GCPs) required for accurate mapping, thereby minimizing the time spent in hazardous environments. Despite fewer GCPs, the results showed that the mapping accuracy remained close to that of geodetic reference data, making the method effective for real-world applications in landslide-prone areas.

The study found that placing GCPs vertically or diagonally along the slope more significantly improved the accuracy compared to top-only GCP placement. The straight vertical GCP configuration yielded the best results in terms of minimizing errors and aligning closely with the geodetic data. Additionally, a slope stability analysis using the Finite Element Method (FEM) showed that the straight-line GCP configuration resulted in the most stable slope model with a safety factor close to that of the GPS geodetic reference, indicating improved landslide prediction.

This research will enable faster, safer, and more cost-effective landslide monitoring, particularly in remote and high-risk areas. Using UAVs with optimized GCP configurations enables the disaster response teams to quickly assess landslide hazards, improve early warning systems, and implement targeted risk mitigation strategies. This study enhances landslide risk management by offering practical and efficient solutions for monitoring and predicting slope instability. To facilitate the understanding of the multi-step procedures conducted in this study, Fig.11 presents a summary diagram of the full workflow. This visual overview integrates all key stages from data acquisition to geotechnical analysis.

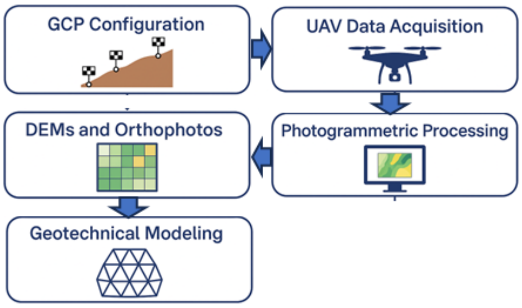

Fig. 11. Summary of the UAV-based slope mapping and geotechnical modeling workflow implemented in this study

3.8. Limitation and future directions

The accuracy of UAV-derived Digital Elevation Models (DEMs) in view of obstructions in photogrammetric capture can be significantly reduced in vegetated areas. Vegetation type and density, such as marram grass or forest undergrowth, have been shown to increase elevation uncertainty [22,23]. UAV models also exhibit lower accuracy compared to Airborne Laser Scanning (ALS) in dense vegetation with omission and commission errors affecting overall model reliability [24]. However, in this study, vegetation interference could be disregarded as the observed slope was a critical, landslide-prone area with minimal to no vegetation cover, allowing clearer terrain capture and more reliable photogrammetric modeling.

Scalability remains another challenge, particularly in large or topographically complex regions. While UAVs enable rapid data collection, coverage limitations and processing demand increase with site size [25,26]. To address these, future work should explore automation strategies such as adaptive UAV altitude control [27] and AI-based terrain correction frameworks [28,29]. Integration with technologies such as GPR or drone swarms can also enhance mapping reliability in inaccessible or hazard-prone areas. Additionally, although this study focuses on a single bare slope, the findings may inform GCP configuration strategies in other steep or hazard-prone terrains, particularly in a sparse vegetation or limited accessibility.

4. Conclusion

This study evaluated the impact of GCP configuration on the accuracy of UAV-based slope modeling and stability analysis. Quantitative analysis revealed that the vertical GCP configuration achieved the lowest total RMSE (5.50 mm), compared to 52.93 mm in the top-only setup and 61.26 mm in the diagonal arrangement. Despite the diagonal layout offering a broader spatial coverage, it introduced slightly higher error. The FEM-based slope stability analysis also confirmed this result with the vertical configuration achieving a Safety Factor (SF) of 1.72, which closely approximated the GPS geodetic reference value of 1.826. In contrast, the top-only GCP setup yielded the lowest SF of 1.269, indicating the least stability, while the diagonal configuration resulted in a moderate SF of 1.514 with improved but still suboptimal strain distribution. The vertical GCP configuration not only enhanced spatial accuracy but also yielded slope stability predictions closest to geodetic references. Future research should evaluate GCP configurations in vegetated and complex terrains where UAV accuracy tends to decline. The optimization of GCP density, integration with real-time geodetic systems, and use of AI-based terrain correction or UAV–GPR platforms may enhance scalability and precision. Improved FEM models based on refined UAV data can further support slope stability analysis and disaster risk mitigation.

Acknowledgements

This research was supported by the DRTPM Grant Program (contract number 056/E5/PG.02.00). PL/2024 and 1043/UN8.2/PG/2024 funded by the Indonesian Ministry of Education, Culture, Research, and Technology.

References

1. E. Cledat, L. V. Jospin, D.A. Cucci and J. Skaloud, *Mapping quality prediction for RTK/PPK-equipped micro-drones operating in complex natural environment*, ISPRS J. Photogramm. Remote Sens. 167 (2020) 24–38.
2. F. Nex, C. Armenakis, M. Cramer, D.A. Cucci, M. Gerke, E. Honkavaara et al., *UAV in the advent of the twenties: Where we stand and what is next*, ISPRS J. Photogramm. Remote Sens. 184 (2022) 215–242.
3. S. Wang, W. Zhang, X. Zhao, Q. Sun and W. Dong, *Automatic identification and interpretation of discontinuities of rock slope from a 3D point cloud based on UAV nap-of-the-object photogrammetry*, Int. J. Rock Mech. Min. Sci. 178 (2024) 105774.
4. F. Nobahar, M.; Salunke, R.; Alzeghoul, O. E.; Khan, M. S.; Amini, *Mapping of Slope Failures on Highway Embankments Using Electrical Resistivity Imaging (ERI), Unmanned Aerial Vehicle (UAV), and Finite Element Method (FEM) Numerical Modeling for Forensic Analysis*, Transp. Geotech. 40 (2023) 100949.
5. K. Tempa, K. Peljor, S. Wangdi, R. Ghalley, K. Jamtsho, S. Ghalley et al., *UAV technique to localize landslide susceptibility and mitigation proposal: A case of Rinchending Goenpa landslide in Bhutan*, Nat. Hazards Res. 1 (2021) 171–186.
6. F. Agüera-Vega, F. Carvajal-Ramírez and P. Martínez-Carricondo, *Assessment of photogrammetric mapping accuracy based on variation ground control points number using unmanned aerial vehicle*, Meas. J. Int. Meas. Confed. 98 (2017) 221–227.
7. P. Martínez-Carricondo, F. Agüera-Vega, F. Carvajal-Ramírez, F.J. Mesas-Carrascosa, A. García-Ferrer and F.J. Pérez-Porras, *Assessment of UAV-photogrammetric mapping accuracy based on variation of ground control points*, Int. J. Appl. Earth Obs. Geoinf. 72 (2018) 1–10.
8. P. Olaszek, I. Wyczałek, D. Sala, M. Kokot and A. Świercz, *Monitoring of the static and dynamic displacements of railway bridges with the use of inertial sensors*, Sensors (Switzerland) 20 (2020) .
9. A.F. Silva, J.M.G. Sotomayor and V.F.N. Torres, *Correlations of geotechnical monitoring data in open pit slope back-analysis - A mine case study*, J. South. African Inst. Min. Metall. 121 (2021) 557–564.
10. Y. Dwikarsa and A. Basith, *Benthic habitats classification using multi scale parameters of GEOBIA on orthophoto images of Karimunjawa waters*, Commun. Sci. Technol. 6 (2021) 55–59.
11. X. Ren, M. Sun, C. Jiang, L. Liu and W. Huang, *An augmented reality geo-registration method for ground target localization from a low-cost UAV platform*, Sensors (Switzerland) 18 (2018) .
12. Y. Erzin and N. Ecemis, *The use of neural networks for the prediction of cone penetration resistance of silty sands*, Neural Comput. Appl. 28 (2017) 727–736.
13. O. de Freitas Neto, O. Santos, F. Franca and R. Severo, *Influence of Compaction Energy and Bentonite Clay Content in the Soil Hydraulic Conductivity*, Appl. Mech. Mater. 851 (2016) 858–863.
14. I. Elkhrachy, *Accuracy Assessment of Low-Cost Unmanned Aerial Vehicle (UAV) Photogrammetry*, Alexandria Eng. J. 60 (2021) 5579–5590.
15. R. Boulanger and I. Idriss, *CPT-Based Liquefaction Triggering Procedure*, J. Geotech. Geoenvironmental Eng. 142 (2015) 4015065.
16. D.M. Seo, H.J. Woo, W.H. Hong, H. Seo and W.J. Na, *Optimization of Number of GCPs and Placement Strategy for UAV-Based Orthophoto Production*, Appl. Sci. 14 (2024) .
17. S. Gindraux, R. Boesch and D. Farinotti, *Accuracy assessment of digital surface models from Unmanned Aerial Vehicles' imagery on glaciers*, Remote Sens. 9 (2017) 1–15.
18. F. Carvajal-Ramírez, F. Agüera-Vega and P.J. Martínez-Carricondo, *Effects of image orientation and ground control points distribution on unmanned aerial vehicle photogrammetry projects on a road cut slope*, J. Appl. Remote Sens. 10 (2016) 034004.
19. F. Niazi, *CPT-Based Geotechnical Design Manual, Volume 1: CPT Interpretation—Estimation of Soil Properties. (Joint Transportation Research Program Publication No. FHWA/IN/JTRP-2021/22)*, I (2021) .
20. H. Zhou, L.M. Wotherspoon, A.C. Stolte and M. Holtrigter, *Assessment and development of empirical correlations between flat plate dilatometer and cone penetration tests for Auckland soils*, New Zeal. J. Geol. Geophys.

(ahead print) (2024) 1–19.

21. T. Tamošiūnas, G. Žaržojus and Š. Skuodis, *Indirect Determination of Soil Young'S Modulus in Lithuania Using Cone Penetration Test Data*, Balt. J. Road Bridg. Eng. 17 (2022) 1–24.
22. I. Papa, M. Popović, L. Hodak, A. Đuka, T. Pentek, M. Hikl et al., *Water and Vegetation as a Source of UAV Forest Road Cross-Section Survey Error*, Forests 16 (2025) 1–18.
23. J. Rotnicka, M. Dłużewski, M. Dąbski, M. Rodzewicz, W. Włodarski and A. Zmarz, *Accuracy of the UAV-Based DEM of Beach–Foredune Topography in Relation to Selected Morphometric Variables, Land Cover, and Multitemporal Sediment Budget*, Estuaries and Coasts 43 (2020) 1939–1955.
24. T. Kloucek, P. Klápšte, J. Marešová and J. Komárek, *UAV-Borne Imagery Can Supplement Airborne Lidar in the Precise Description of Dynamically Changing Shrubland Woody Vegetation*, Remote Sens. 14 (2022) .
25. X. Cui, X. Zhang, Z. Xu and H. Liu, The application of drone tilt photography in large scale topographic mapping, in Fourth International Conference on Geology, Mapping, and Remote Sensing (ICGMRS 2023), 12978 (2024), pp. 3020998.
26. M. Frid, V. Frid and G. Scholar, *Advancements in Drone-based (UAV) Ground Penetrating Radar for Accurate Boundary Mapping between Disturbed Clayey Soil and Natural Rock*, Preprints (2024) 1–12.
27. C.S. Nijjar, S. Singh, T. Jaiswal and S. Kalra, *High-Resolution Mapping of Forest Canopy Cover Using UAV and Sentinel-2*, in *Proceedings of UASG 2021: Wings 4 Sustainability. UASG 2021. Lecture Notes in Civil Engineering*, K. Jain, V. Mishra and B. Pradhan, eds., Springer, Cham, 2023, pp. 331–341.
28. J. Na, K. Xue, L. Xiong, G. Tang, H. Ding, J. Strobl et al., *UAV-based terrain modeling under vegetation in the chinese loess plateau: A deep learning and terrain correction ensemble framework*, Remote Sens. 12 (2020) 1–18.
29. T.N. Nguyen, T.B. Nguyen, T. Van Chien and T.H. Nguyen, *Utilizing Deep Reinforcement Learning to Control UAV Movement for Environmental Monitoring*, Int. J. Electr. Electron. Eng. Telecommun. 12 (2023) 317–325.